Retracking CryoSat-2, Envisat, and Jason-1 Radar Altimetry Waveforms for Optimal Gravity Field Recovery

Emmanuel S. Garcia
David T. Sandwell
Scripps Institution of Oceanography, University of California, San Diego

Submitted to: *Geophysical Journal International*, November 30, 2012

Abstract

Improving the accuracy of the marine gravity field requires both increased altimeter range precision and dense track coverage. After a hiatus of more than 15 years, a wealth of suitable data is now available from the satellites CryoSat, Envisat, and Jason-1. In particular, Cryosat has a new synthetic aperture radar (SAR) mode that provides a more complex waveform shape that should result in higher range precision. For this new mode we derived a simple analytic model for the shape of the SAR waveform and tuned the least-squares retracking approach to achieve optimal range precision. As for the conventional modes on all these satellites, the range precision of data from these can be significantly improved with respect to the conventional techniques used in operational oceanography by retracking the altimeter waveforms using an algorithm that is optimized for range precision at the expense of other parameters such as significant wave height. We have demonstrated that a two-pass retracking algorithm that was originally designed for data from prior missions (ERS-1 and Geosat) also improves precision on all three of the new satellites by about a factor of 1.5. The improved range precision and dense coverage from CryoSat, Envisat, and Jason-1 combined with data from ERS-1 and Geosat will to lead to a substantial increase in the accuracy of the marine gravity field.

Introduction

Marine gravity anomalies derived from radar altimeter measurements of ocean surface slope are the primary data for investigating global tectonics and seafloor bathymetry. At horizontal scales less than 200 km, the ocean surface undulates following the topography of the seafloor, and thus altimetry provides seafloor maps in uncharted areas. While there have been several recent global gravity missions such as CHAMP, GRACE, and GOCE that provide extraordinarily accurate measurements of gravity, their spatial resolution is

worse than 200 km because they sense the gravity field from orbital altitudes. Radar altimeters sense the gravity field at the ocean surface so they can recover spatial scales as small as ~6 km, which is the limit provided by upward continuation of the gravity field at seafloor depths through the overlying ocean layer. The scientific rationale for improved gravity is fairly mature and a set of papers related to this topic was published in a special issue of Oceanography [*Smith*, 2004], entitled *Bathymetry from Space*. These studies show that achieving an accuracy of 1 milligal (mGal) at a horizontal resolution of 6 km would enable major advances for a large number of basic science and practical applications.

For recovery of the static marine gravity field, the critical measurement is the slope of the ocean surface. Laplace's equation combined with Bruns' formula shows that one microradian (μrad) of ocean surface slope roughly corresponds to 1 mGal of gravity anomaly. Therefore, achieving this 1 μrad threshold requires a radar altimeter range having a precision of 6 mm over 6 km horizontal distance. This precision could be derived from a single profile or a stack of repeated profiles. Ocean surface slope can be estimated by differencing height measurements along satellite altimeter profiles so absolute range accuracy is largely irrelevant. Indeed the usual corrections and ancillary data that are needed to recover the temporal variations in ocean surface height associated with currents and eddies are largely unimportant for the recovery of the gravity field because the slope of these corrections is far less than the slope error in the radar altitude measurement.

In addition to high range precision, the accuracy of the global marine gravity field depends on dense track spacing, which needs to be less than the desired resolution of 6 km. Current gravity fields having accuracies of 3-5 mGal (e.g., S&S V18 [*Sandwell and Smith*, 2009] and DNSC08 [*Andersen et al.,* 2009]) are based primarily on dense track coverage from 18 months of Geosat/GM data collected in 1985-86 and 12 months of ERS-1/GM collected in 1995-96. Since those missions there have been several advances in radar altimeter technology, but all the newer satellites have been placed in a repeat orbit configuration having wide track spacing. This wide track spacing configuration (i.e. short repeat cycle) is optimal for recovering changes in ocean surface height associated

with currents and tides [*Fu and Cazenave*, 2001] but provides little new gravity information. The short repeat orbit altimeters include Geosat/ERM, 1986-1989; ERS-1, 1991-1995; Topex/Poseidon, 1992-2006; ERS-2, 1995-2010; GFO, 1998-2008; Jason-1, 2001- 2012; Envisat, 2002-2012; and Jason-2, 2008-present.

Achieving the desired 1 mGal accuracy of the global marine gravity will require new altimeter measurements having both dense ground tracks and high range precision. CryoSat-2 is the first altimeter in the past 15 years that offers advancements in both of these capabilities [*Wingham et al.*, 2006]. CryoSat-2 was successfully launched in February of 2010 and has routinely collected altimetry data over ice, land, and ocean since July 2010. The satellite has a long 369-day repeat cycle resulting in an average ground track spacing of 3.8 km at the equator (Figure 1). Over the ocean, the altimeter is operated in three modes, which produce distinct returned signals. The standard *Low Rate Mode* (LRM) is the conventional pulse-limited radar altimeter mode that has been used by all previous radar altimeters (black lines in Figure 1). This mode requires a relatively low data bandwidth and is used continuously over all ice-free ocean areas. The new *Synthetic Aperture Radar* (SAR) mode is used over ocean areas where sea ice is prevalent as well as a few small test areas (green lines in Figure 1). In this mode the radar sends a burst of pulses with an interval of 50 μs. The returning echoes are summed coherently in the along-track direction forming an 86-m long synthetic aperture. This results in a footprint that is beam-limited and narrow (0.29 km) in the along-track direction and pulse-limited and broad (1.5-3 km) in the cross-track direction [*Ford and Pettengill*, 1992; *Raney,* 1998]. In addition, the echoes are sorted by Doppler frequency, allowing for the formation of distinct radar-illuminated beams along the satellite ground track. The locations of these beams can be described by a "look" angle measured with respect to the satellite reference frame. The return signals from multiple beams can be combined after performing range migration, in a process termed "multilooking", or "multilook averaging".

The SAR-mode is used over relatively flat areas of floating sea ice to measure ice freeboard. If this mode were to be used extensively over the ice-free ocean it could (theoretically) provide a factor of 2 improvement in range precision which could translate

into a factor of 2 improvement in the global gravity models [*Raney et al.*, 2003; *Smith and Sandwell*, 2004; *Louis et al.*, 2010]. There is a third mode of operation to measure elevation and cross-track slope over land ice surfaces where there is significant topographic slope. In this mode, the two antennas on CryoSat-2 are used to form a cross-track interferometer. This is called the *SAR/Interferometric Radar Altimeter* (SARIN) mode. Both the SAR and SARIN modes require a very high bandwidth data link to the ground stations.

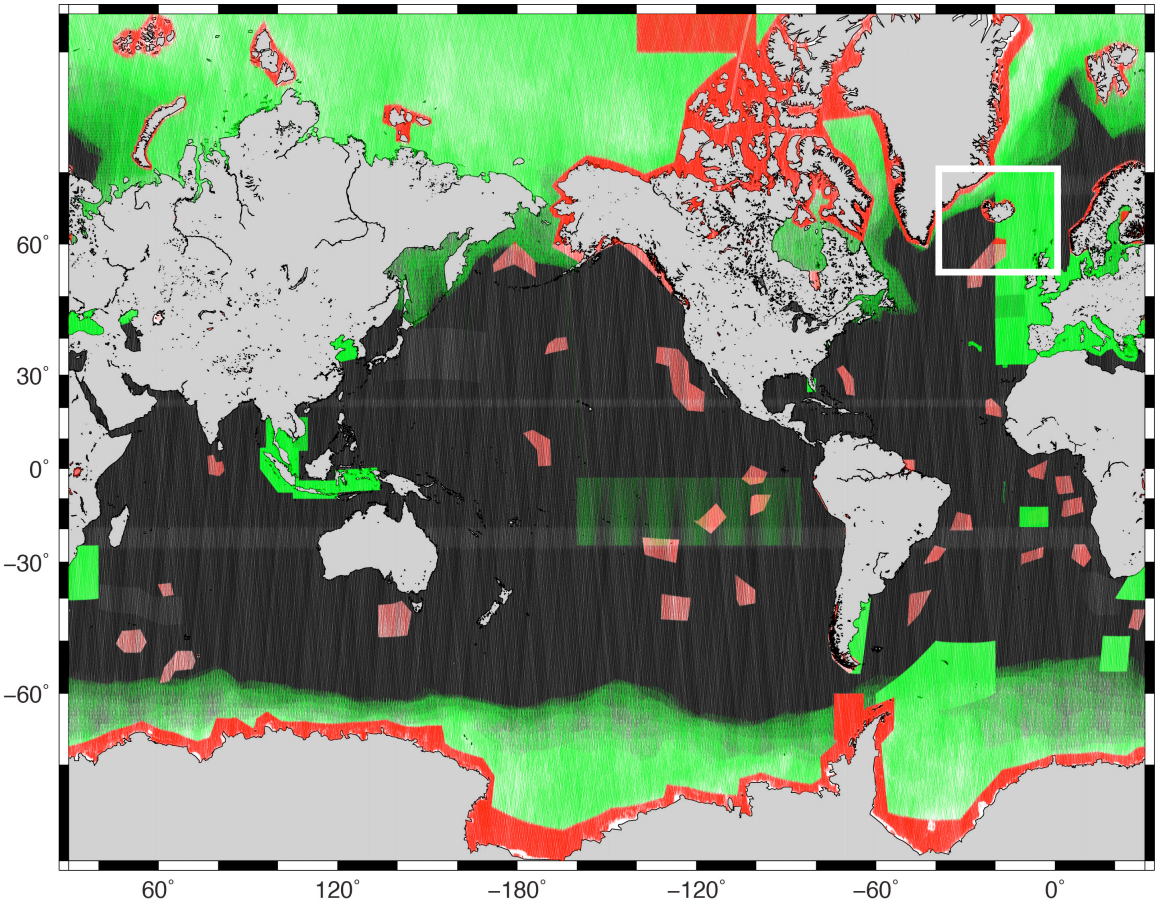

Figure 1. Ground tracks of the first 26 months of CryoSat altimeter data in its three modes of operation LRM (black), SAR (green), and SARIN (red). White box shows area for LRM and SAR along-track 1 Hz noise and repeat-track coherence estimation.

One focus of this study is the development of methods to track the return waveforms of the CryoSat-2 ocean data in the new SAR mode. In addition, we provide results on the application of the 2-pass retracking method [*Sandwell and Smith*, 2005] to the new

standard-model altimetry data being provided by CryoSat, Envisat, and Jason-1. Since we are mainly interested in measuring ocean surface slope along the track of the satellite profile, our approach is optimized for range precision at the expense of other information that could be extracted from the radar echoes such as significant wave height and wind speed. We first review the theory for retracking the standard LRM waveform data. Then using the same methodology we develop an analytic formula for the shape of the SAR waveforms under the ideal conditions of low significant wave height and small radar mispointing angle. We show that this analytical model is an adequate approximation to the more fully developed waveform models that also include the effects of multilooking and radar mispointing [*Wingham et al.,* 2004*; Cotton et al.,* 2010]. Moreover we approximate the trailing edge decay caused by the finite beamwidth of the antenna using a simple exponential decay [*Amarouche et al.*, 2004]. Finally we evaluate the range precision and along-track resolution of the LRM and SAR data from CryoSat-2 through a comparison with the best available gravity models as well as noise estimates from other non-repeat orbit altimeters (Geosat, ERS-1, Envisat, and Jason-1). Our analysis provides new estimates of range precision from Envisat and Jason-1 using the 2-parameter retracking method first developed for ERS-1 and Geosat [*Sandwell and Smith*, 2005]. The results suggest that if CryoSat-2 continues to collect data for three full years, the accuracy of the global gravity field will improve by a factor of 2.

Model Waveforms

The shape of the return radar waveforms collected by the altimeter can be described as a function of the delay time τ, which is the sampling time t referenced to the arrival time of the waveform t_0, such that $\tau = t - t_0$. The power versus delay time for the model radar return pulse $M(\tau)$ is given by the triple convolution of the source time function $P(\tau)$, the effective area of the ocean illuminated versus time $A(\tau)$, and the ocean surface roughness function $G(\tau)$ [*Amarouche et al.*, 2004]

$$M(\tau) = P(\tau) * A(\tau) * G(\tau). \quad (1)$$

The source time function has the form of a $\boldsymbol{sinc}^2\left(\frac{\pi\tau}{\tau_p}\right)$ because the pulse is formed by deconvolution of a frequency modulated chirp. The bandwidth of the chirp is 320 MHz. This results in an effective pulse length of 3.125 nanoseconds for an effective range resolution of the radar of .4667 m. To simplify the convolution integrals, it is customary to approximate the *sinc*^{2} function with a Gaussian function of the form

$$P(\tau) = \frac{1}{\sigma_p\sqrt{2\pi}}\exp\left(\frac{-\tau^2}{2\sigma_p^2}\right) \tag{2}$$

where σ_p is the standard deviation of the pulse length given by $\sigma_p = 0.4541\tau_p$ [*Brown*, 1977]. Note the integral of this power over time is normalized to one. The roughness of the ocean surface due to ocean waves is also well approximated by a Gaussian function [*Stewart*, 1985]

$$G(\tau) = \frac{1}{\sigma_h\sqrt{2\pi}}\exp\left(\frac{-\tau^2}{2\sigma_h^2}\right) \tag{3}$$

where σ_h is related to the significant wave height h_{swh} by

$$\sigma_h = \frac{h_{swh}}{4c} \tag{4}$$

where c is the speed of light. The order of the triple convolution given in equation (1) is unimportant so we begin by convolving the Gaussian approximation to the source function with the Gaussian wave height distribution resulting in

$$P(\tau) * G(\tau) = \frac{1}{\sigma\sqrt{2\pi}}\exp\left(\frac{-\tau^2}{2\sigma^2}\right) \tag{5}$$

where $\sigma^2 = \sigma_h^2 + \sigma_p^2$.

The final convolution, of the Gaussian pulse with the effective area of the ocean illuminated by the radar, determines the shape of the model waveform. Since we are most interested in measuring the arrival time of the return pulse, our analysis is not concerned with the amplitude of the pulse. In addition we will make the assumption that the diameter of the pulse-limited footprint is much less than the diameter of the antenna beam pattern so the variation in antenna power within the pulse-limited area is small and can be approximated as a constant. Later, we will partly correct for the varying antenna pattern by multiplying by an exponential decay function with an empirically determined constant. This approximation will break down when the off-nadir pointing angle reaches a large fraction of the antenna beam angle.

Area of Ocean Reflection - Brown Model

Over the ocean the CryoSat altimeter is operated in two modes (Figure 2). The standard low rate mode (LRM) has pulses having approximately spherical wavefronts. These reflect from an annulus on the ocean surface having an area $A(r) = 2\pi r dr$ where r is the radius of the annulus and *dr* is the width of the annulus. The approximate radius of the pulse versus time is given by [*Walsh,* 1977; *Hayne* 1980; *Stewart*, 1985]

$$r(\tau) \cong (hc\tau)^{1/2} H(\tau) \tag{6}$$

where $H(\ )$ is the Heaviside step function. While the radius of the annulus increases as the square root of time, the thickness of the annulus per unit time decreases as the square root of time

$$dr = \frac{1}{2}\left(\frac{hc}{\tau}\right)^{1/2} d\tau \ . \tag{7}$$

so the area of the annulus is uniform after the arrival of the pulse.

$$A(\tau) = \pi hcH(\tau)d\tau \,. \tag{8}$$

Later we'll include a slow exponential decay in this effective area versus time function to approximate the finite beamwidth of the antenna pattern.

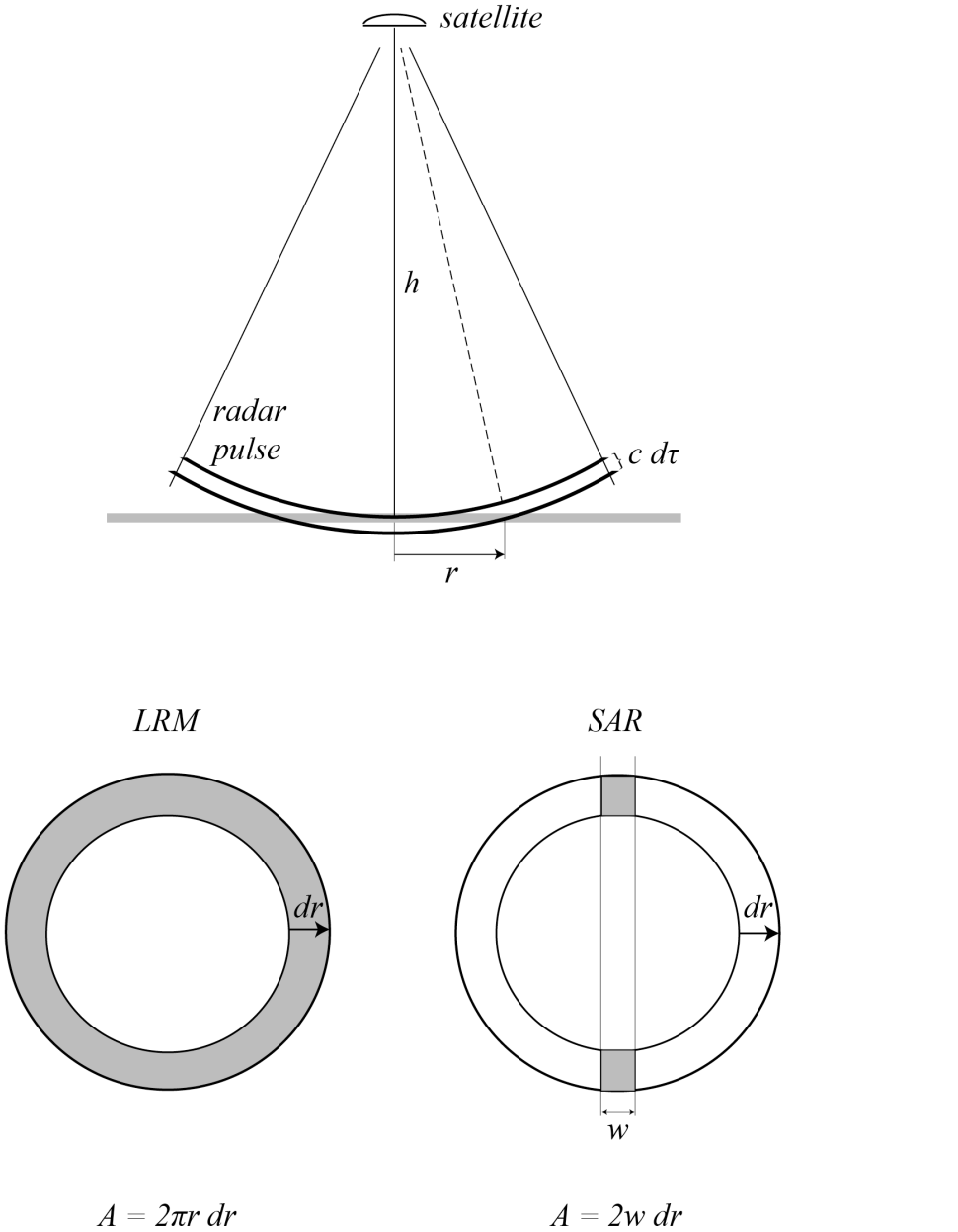

Figure 2. Interaction of a radar pulse with a flat surface. (a) Area illuminated in standard LRM mode after the arrival of the pulse. (b) Area illuminated by the synthetic aperture radar (SAR) method where *w* is the effective width of the focused beam in the along-track direction.

The final step in generating the model waveform is to convolve the effective area versus time with the Gaussian pulse function

$$M(\tau) = P(\tau) * G(\tau) * A(\tau) = \frac{hc}{\sigma}\sqrt{\frac{\pi}{2}}\int_{-\infty}^{\infty} \exp\left(\frac{-(\tau-\tau')^2}{2\sigma^2}\right) H(\tau')\, d\tau' \,. \tag{9}$$

This can be written as

$$M(\tau) = \frac{hc}{\sigma}\sqrt{\frac{\pi}{2}}\int_{0}^{\infty} \exp\left(\frac{-(\tau-\tau')^2}{2\sigma^2}\right) d\tau' \,. \tag{10}$$

Note that the definition of the error function is

$$erf(\eta) = \frac{2}{\sqrt{\pi}}\int_{0}^{\eta} \exp\left(-\xi^2\right) d\xi \,. \tag{11}$$

Let $\xi = \dfrac{\tau'-\tau}{\sqrt{2}\sigma}$ so $d\tau' = \sqrt{2}\sigma d\xi$. The integral becomes

$$M(\tau) = hc\sqrt{\pi}\left[\int_{\frac{-\tau}{\sqrt{2}\sigma}}^{\infty} \exp\left(-\xi^2\right) d\xi\right] = hc\sqrt{\pi}\left[\int_{0}^{\infty} \exp\left(-\xi^2\right) d\xi + \int_{0}^{\frac{\tau}{\sqrt{2}\sigma}} \exp\left(-\xi^2\right) d\xi\right] \tag{12}$$

The final familiar result is

$$M(\tau) = \frac{hc\pi}{2}\left[1 + erf(\eta)\right] = \frac{A}{2}\left[1 + erf\left(\frac{\tau}{\sqrt{2}\sigma}\right)\right] \tag{13}$$

where A is the amplitude and $\eta = \frac{\tau}{\sqrt{2}\sigma}$. The partial derivatives of the model with respect to τ, σ, and A are

$$\frac{\partial M}{\partial \tau} = \frac{-A}{\sigma\sqrt{2\pi}} e^{-\eta^2} \tag{14}$$

$$\frac{\partial M}{\partial \sigma} = \frac{-A}{\sigma\sqrt{\pi}} \eta e^{-\eta^2} \tag{15}$$

$$\frac{\partial M}{\partial A} = \frac{M}{A} \tag{16}$$

, respectively.

SAR Model

A similar approach is used to develop the waveform shape for the SAR model as well as its derivatives with respect to the model parameters. When CryoSat is operated in the SAR mode, the footprint is focused to an effective width of w in the along-track direction [*Raney*, 1998; *Wingham et al*., 2004]. In this case the area of the illuminated ocean surface is approximately given by

$$A(r) = 2wdr \tag{17}$$

when $w << r$ (Figure 2), implying that the illuminated beam pattern can be treated as close to rectangular. Later we will evaluate the error in this approximation. As shown above, when dr is expressed in terms of the delay time it is

$$dr = \frac{1}{2}\left(\frac{hc}{\tau}\right)^{1/2} d\tau \,. \tag{18}$$

So the area versus delay time function is given by

$$A(\tau) = w\left(\frac{hc}{\tau}\right)^{1/2} d\tau \tag{19}$$

The model return waveform is the convolution of the Gaussian pulse with this area versus time function

$$M(\tau) = P(\tau) * G(\tau) * A(\tau) = \frac{w\sqrt{hc}}{\sigma\sqrt{2\pi}} \int_{-\infty}^{\infty} \exp\left(\frac{-(\tau-\tau')^2}{2\sigma^2}\right) \tau'^{-1/2} H(\tau') d\tau' . \tag{20}$$

After a bit of algebra one arrives at

$$M(\tau) = C \exp\left(\frac{-\tau^2}{2\sigma^2}\right) \int_0^{\infty} \tau'^{-1/2} \exp\left[-\left(\frac{1}{2\sigma^2}\right)\tau'^2 + \left(\frac{\tau}{\sigma^2}\right)\tau'\right] d\tau' \tag{21}$$

where $C = \frac{w\sqrt{hc}}{\sigma\sqrt{2\pi}}$.

Note that this integral can be performed analytically using the following formula [*Gradshteyn*, 1980]

$$\int_0^{\infty} \tau^{-1/2} \exp\left(-\beta\tau^2 - \gamma\tau\right) d\tau = (2\beta)^{-1/4} \Gamma(1/2) \exp\left(\frac{\gamma^2}{8\beta}\right) D_{-1/2}\left(\frac{\gamma}{\sqrt{2\beta}}\right) \tag{22}$$

where $D_{-1/2}(x)$ is the parabolic cylinder function and $\Gamma(x)$ is the gamma function for some argument x. Note that $\Gamma(1/2) = \sqrt{\pi}$. We make the substitutions $\beta = \frac{1}{2\sigma^2}$ and $\gamma = \frac{-\tau}{\sigma^2}$ so the integral becomes

$$\int_0^\infty \tau'^{-1/2} \exp\left[-\left(\frac{1}{2\sigma^2}\right)\tau'^2 + \left(\frac{\tau}{\sigma^2}\right)\tau'\right] d\tau' = \sqrt{\pi\sigma}\exp\left(\frac{\tau^2}{4\sigma^2}\right) D_{-1/2}\left(\frac{-\tau}{\sigma}\right). \tag{23}$$

The final result is

$$M(\tau) = w\left(\frac{hc}{2\sigma}\right)^{1/2} \exp\left(-\frac{\tau^2}{4\sigma^2}\right) D_{-1/2}\left(\frac{-\tau}{\sigma}\right) = A\sigma^{-1/2}\exp\left(-\frac{\tau^2}{4\sigma^2}\right) D_{-1/2}\left(\frac{-\tau}{\sigma}\right). \tag{24}$$

As in the case of the Brown model, we would like to compute the partial derivatives of the model with respect to τ , σ , and *A*. The derivative of the model with respect to *A* is simply

$$\frac{\partial M}{\partial A} = \frac{M}{A}. \tag{25}$$

To compute the other derivatives we make use of the identity [*Temme,* 2010]

$$\frac{\partial}{\partial z}\left[\exp\left(-\frac{1}{4}z^2\right) D_{-1/2}(z)\right] = -\exp\left(-\frac{1}{4}z^2\right) D_{1/2}(z). \tag{26}$$

Now we let $z = -\tau/\sigma$. Using the chain rule, the derivative with respect to τ becomes

$$\frac{\partial M}{\partial \tau} = \frac{\partial M}{\partial z}\frac{\partial z}{\partial \tau} \tag{27}$$

where $\frac{\partial z}{\partial \tau} = \frac{-1}{\sigma}$ and $\frac{\partial z}{\partial \sigma} = \frac{\tau}{\sigma^2}$.

Using the expression above, the derivative of the model with respect to z is

$$\frac{\partial M}{\partial z} = -A\sigma^{-1/2}\exp\left(-\frac{1}{4}z^2\right)D_{1/2}(z). \tag{28}$$

Combining terms one gets

$$\frac{\partial M}{\partial \tau} = A\sigma^{-3/2}\exp\left(-\frac{1}{4}z^2\right)D_{1/2}(z). \tag{29}$$

A similar approach can be used to calculate the derivative with respect to σ.

$$\frac{\partial M}{\partial \sigma} = \frac{\partial M}{\partial z}\frac{\partial z}{\partial \sigma}. \tag{30}$$

By rewriting $M = A\sigma^{-1/2}\exp\left(-\frac{1}{4}z^2\right)D_{-1/2}(z)$ we can form the derivative as the sum of two terms. The first term is

$$\left(\frac{\partial M}{\partial \sigma}\right)_1 = -\frac{1}{2}A\sigma^{-3/2}\exp\left(-\frac{1}{4}z^2\right)D_{-1/2}(z). \tag{31}$$

The second term is

$$\left(\frac{\partial M}{\partial \sigma}\right)_2 = -A\tau\sigma^{-5/2}\exp\left(-\frac{1}{4}z^2\right)D_{1/2}(z). \tag{32}$$

Combining terms we find

$$\frac{\partial M}{\partial \sigma} = -A\sigma^{-3/2}\exp\left(-\frac{1}{4}z^2\right)\left[\frac{1}{2}D_{-1/2}(z) + \frac{\tau}{\sigma}D_{1/2}(z)\right]. \tag{33}$$

In summary we have the following results for the SAR waveform model and its derivatives with respect to τ, σ, and A

$$M = A\sigma^{-1/2}\exp\left(-\frac{1}{4}z^2\right)D_{-1/2}(z) \tag{34}$$

$$\frac{\partial M}{\partial \tau} = A\sigma^{-3/2}\exp\left(-\frac{1}{4}z^2\right)D_{1/2}(z) \tag{35}$$

$$\frac{\partial M}{\partial \sigma} = -A\sigma^{-3/2}\exp\left(-\frac{1}{4}z^2\right)\left[\frac{1}{2}D_{-1/2}(z) - zD_{1/2}(z)\right] \tag{36}$$

$$\frac{\partial M}{\partial A} = \frac{M}{A} \tag{37}$$

where $z = -\tau/\sigma$. As discussed in the next section, the model must also be multiplied by a function having an exponential decay for positive τ to account for the finite beamwidth of the radar antenna.

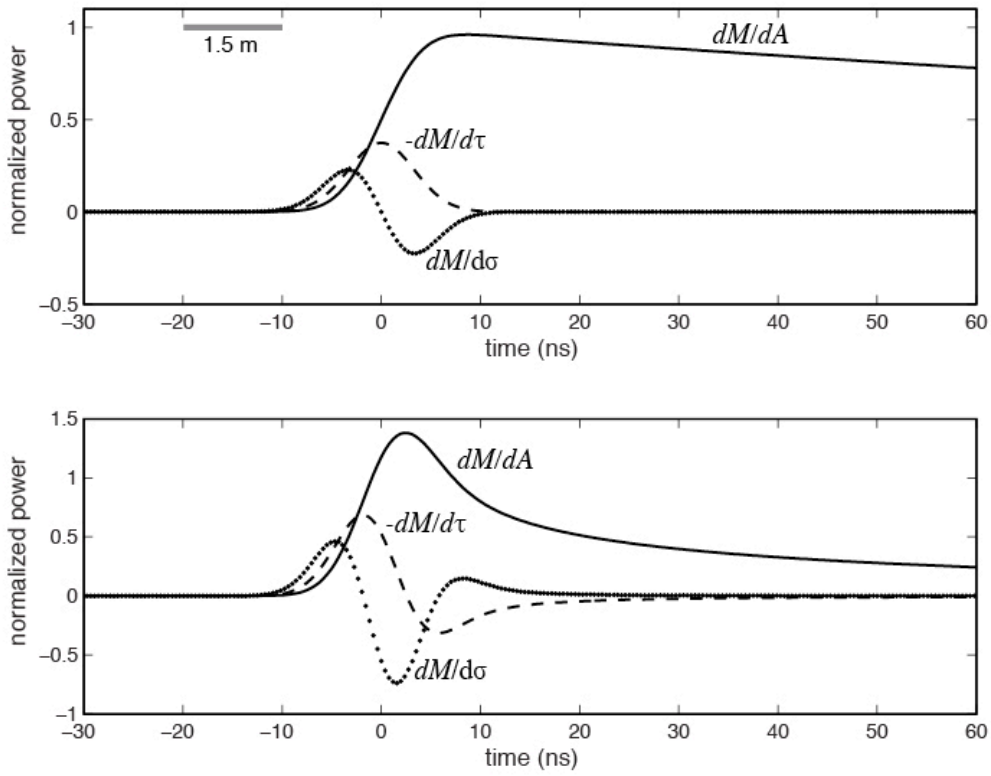

Figure 3. (upper) Brown model waveform including the exponential approximation to the trailing edge decay for a 2 m SWH. Model derivatives with respect to arrival time (dashed) and rise time (dotted) are also shown. (lower) SAR model waveform including the exponential approximation to the trailing edge decay for a 2 m SWH. Model derivatives are also shown.

Assessment of Approximate SAR Model

This derivation assumes a nadir-pointing radar and does not include the complications due to multilook averaging. However, mispointing and multilook averaging can have important effects on the shape of the model waveform [*Wingham et al.,* 2004; *Cotton et al.,* 2010]. To date there is no completely analytical expression for the shape of the multilooked SAR model waveform and its partial derivatives with respect to arrival time, SWH, and off-nadir pointing angle. Computation of the more complete numerical model [*Phalippou and Enjolras,* 2007] involves multiple numerical integrations and thus the only practical retracking approach will involve pre-computing models and partial derivatives for a suite of model parameters and building a retracking code that rapidly retrieves template models. This purely numerical approach will require extensive development and testing. In our marine gravity analysis we are mainly interested in the along-track slope of the ocean surface and are not interested in estimating SWH. We show next that under certain conditions of moderate SWH and small off-nadir pointing angle, the analytic model (eqn. 34) is adequate for estimating along-track slope to better than 1 μrad. Moreover because the formulation has analytic derivatives with respect to the model parameters, we can retrack 12 months of CryoSat SAR waveforms in about a day on a desktop computer. This rapid analysis enables us to explore and refine least squares approaches and waveform weighting functions as well as parameter reduction approaches [e.g., *Sandwell and Smith* 2005]. We have found that whether for LRM or SAR-mode data, subtle factors such as the number of 20 Hz waveforms that are assembled in a single least-squares fit or the amount of along-track smoothing of the SWH between the 3-parameter and 2-parameter retracking can have a significant effect on the along-track slope precision.

To assess the accuracy of the simple analytical model for estimating waveforms, we used our approach to retrack waveforms generated from the full-multilooked theoretical model including variations in SWH (0.5 to 8 m), and off-nadir roll angle (0.0˚ to 0.30˚) [personal communication, SAMOSA Project, Salvatore Dinardo, 2012]. The simulated waveform data was provided at a sampling of 1.5625 nanoseconds (or half the original tracking gate interval) to match the new L1b SAR format being provided by ESA. The

first test involved retracking a single-looked SAMOSA waveform over the range of SWH and off-nadir roll angle shown in Figure 4a. When the off-nadir roll is 0˚, the analytic model and SAMOSA model waveforms agree in shape to better than 1 part in 1000 at all gates for the full range of SWH. An exponential trailing edge decay function of the form $\exp(-\tau/\alpha)$ was used to improve the fit where the best-fit α^{-1} was 0.0149 gate^{-1}. The arrival time estimated from the fit of the analytical model to the nadir-pointing SAMOSA data agreed to better than 1 mm in absolute range. The σ parameter from the least squares model fit shows a good linear relationship with the SWH for the SAMOSA data with a misfit at smaller SWH due to the finite width of the point target response function not included in the analytic formulation (Figure 4b). This comparison confirms that these two formulations agree in this single-look, nadir-pointing case.

The least-squares fit of the analytic model to the multilooked (253 looks) SAMOSA waveform data show good visual fits for larger SWH but a poor fit at the base of the leading edge of the waveform (-15 to -5 ns) for an SWH of 0.5 m. This feature is referred to as the "toe" of the waveform. Multilooking is essentially an incoherent sum of the fore- and aft- looking beams in order to improve the signal-to-noise ratio of the 20 Hz waveforms [*Wingham et al*., 2004]. Prior to summation, the off-nadir beams are shifted in range according to their extra path length compared to the nadir beam. Multilook averaging causes an overall smoothing of the waveform. The broad off nadir beams create the "toe" at the leading edge that is not available in the analytic model. It should be noted that this multilook processing is designed for recovery of ice topography where multimeter excursions from the smooth geoid are common. Therefore the beneficial effects of a more robust waveform amplitude are more important than retaining the sharpest possible leading edge.

Although the multilook averaging has a significant effect on the entire shape of the waveform, it is nevertheless, still possible to adjust the parameters of the analytic model to provide a good match. The question is how does this adjustment of the wrong-shaped analytic model affect the recovered parameters of arrival time and rise time? Remarkably, in the case of zero roll angle, the recovered arrival time agrees to better than 1 mm with the actual arrival time over the full range of SWH. However, the estimated rise time is over-estimated with respect to the true SWH, especially when the SWH is low

as shown in Figure 4b. Indeed, based on this analysis one could conclude that recovery of SWH less than 2 m will be challenging and perhaps impossible because the multilooking smooths the waveform in a way that is well approximated by convolution of a 2-m Gaussian wave height distribution. The remarkable conclusion is that the arrival time estimated by fitting an analytic model to a multilooked waveform, having zero roll angle, is accurate to better then 1 mm. Of course when the actual noisy waveforms are modeled, the estimated arrival time parameter will be less accurate but this analysis suggests that there is not a significant range bias caused by multilooking.

The more important issue is the arrival time error caused by a non-zero off-nadir roll angle. Again we can use the simulated SAMOSA data to estimate the magnitude of this effect. The results of this analysis are shown in Figure 5 where we plot the arrival time error from the fit of the analytic model as a function of SWH and off-nadir roll angle. We performed this analysis using both single look (Figure 5a) and multilooked (Figure 5b) waveforms and the results are remarkably similar. When the off-nadir roll angle is less than 0.02˚, the error is less than 7 mm. Following the approach of *Smith and Scharroo* [2011], we calculated the off-nadir roll angle from the spacecraft orientation data provided in the L1b product for the month of April, 2011. A constant 0.085˚ roll bias was included in the analysis. A cumulative histogram versus off nadir roll shows that 90% of the data were acquired when the off-nadir roll angle is less than 0.12˚ (Figure 5c). Our least-squares fits to the SAMOSA waveforms having off-nadir roll of 0.12˚ show misfits of 1 mm error at SWH of 1 m rising to 3.6 mm at an SWH of 2 m and in the most extreme case of SWH of 6 m, the error is 23 mm. Our objective for slope precision is 1 μrad. To determine the maximum slope error that could be caused by this range error associated with the roll angle we also calculated the roll rate for an example SAR pass across the Pacific. The maximum roll rate is 1.5×10^{-4} degrees per km along the satellite track. Based on the analysis of the range error of 23 mm caused by a change in roll angle of 0.12 deg., we calculate an upper bound on slope error of 0.029 μrad. This upper bound is 35 times smaller than our accuracy goal of 1 μrad so this error source is not important for construction of marine gravity. However, it is likely and possible to have a range error of 23 mm over the length of a few thousand kilometers. This magnitude of error is significant for construction of sea surface height models. So we reiterate that our

retracking approach, which does not account for mispointing error, is adequate for measuring sea surface slope but not height.

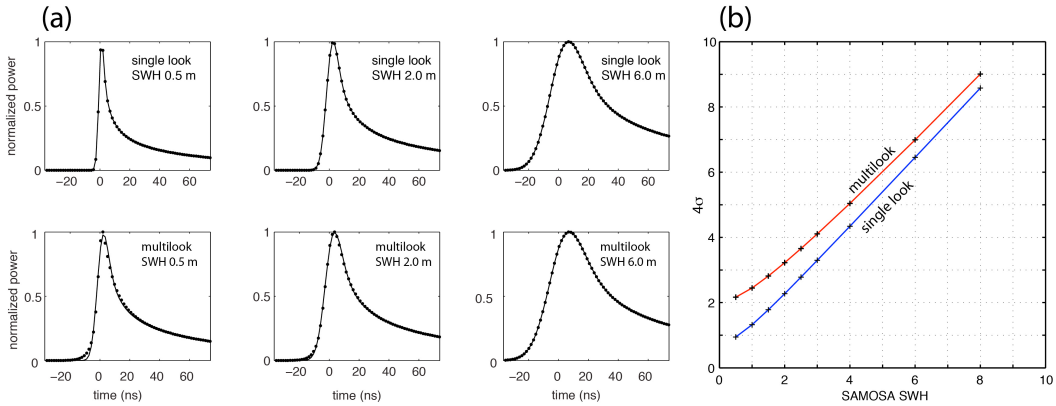

Figure 4. (a) Fit of analytic model to SAMOSA data (black dots) for single look (top row) and multilooked waveforms (bottom row) for wave heights of 0.5, 2.0, and 6.0 m and 0˚ off-nadir roll angle. Note the poor fit of the analytic model to the "toe" of the multilooked waveform when the SWH is low (0.5 m). (b) Comparison of the rise time 4σ from the best-fit analytic model to the SWH for the single- and multi-looked waveforms. Except at low SWH, the rise time of the analytic model 4σ shows a good one-to-one relationship with the SWH. Meanwhile, the relationship for the multilooked waveform is not one-to-one suggesting that the analytic model accommodates the shape of the multilooked waveform by increasing the model rise time σ.

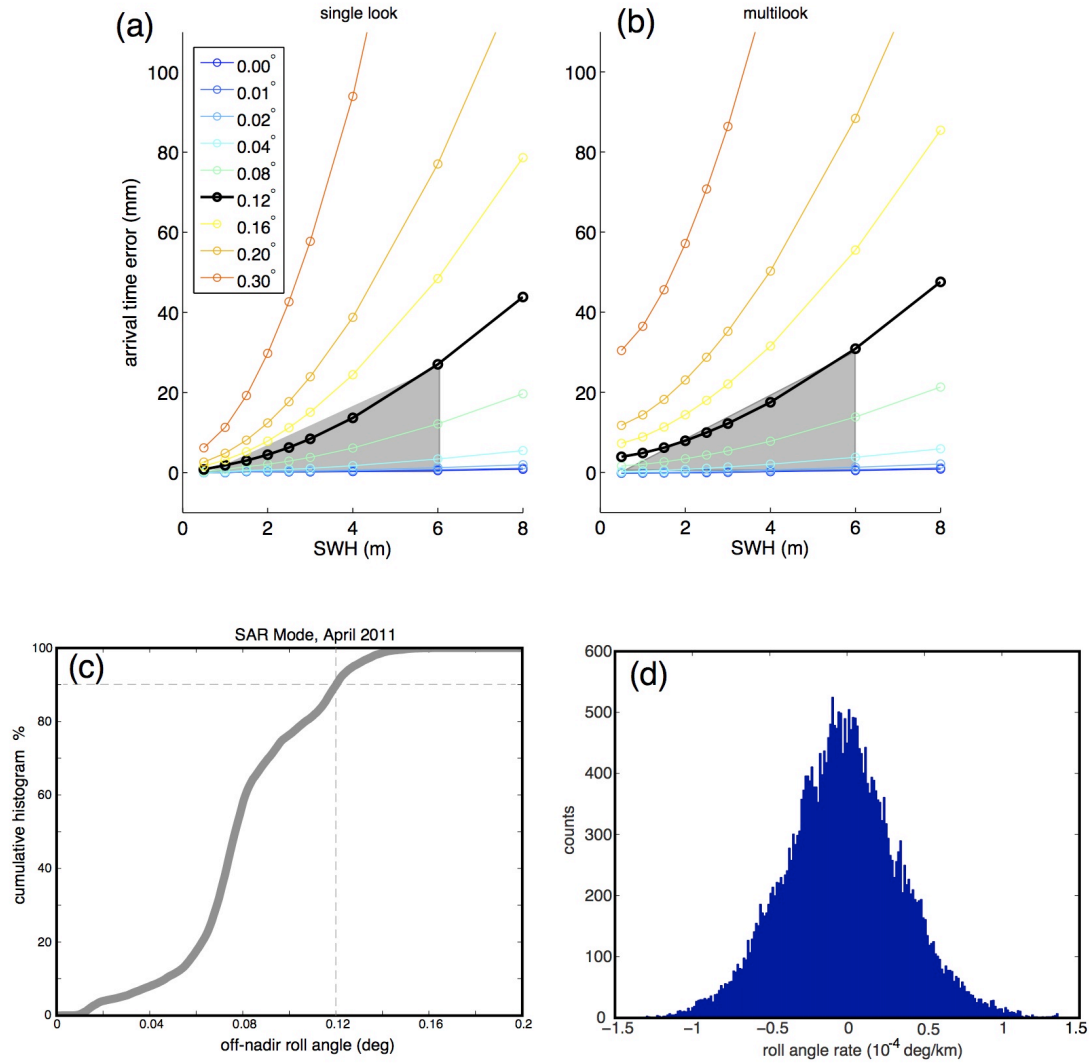

Figure 5 Error in arrival time for analytic model as a function of SWH for a range of off-nadir roll angles. Fits to both single- and multi-looked waveforms are shown. (c) Cumulative histogram of the absolute value of the off-nadir roll angle. A roll bias of 0.085˚ has been included [*Smith and Scharroo,* 2011]. Grey shading shows the restricted parameter ranges to be used for gravity analysis. (d) Roll angle rate for a SAR pass across the Pacific.

Least Squares Analysis

Using these two functional forms for the LRM (eqn. 14) and SAR (eqn. 34) waveforms, we applied a standard Newton iterative least squares method to optimally estimate the 4 parameters of A-amplitude, t_0-arrival time, σ-rise time, and α-trailing edge decay [e.g., *Thibaut et al.*, 2010]. The 4-parameter approach is commonly called maximum likelihood estimator (MLE4); if the trailing edge decay parameter is held fixed, then the approach is called MLE3. Two previous studies [*Maus et al.,* 1998;

Sandwell and Smith, 2005] showed that when a weighted MLE3 analysis is performed, there is a strong covariance between the estimate of arrival time and rise time resulting in a relatively noisy estimate of arrival time. Moreover, these studies showed that if the rise time parameter is held to a fixed value, derived from about 40 km of along-track waveforms, the noise in arrival time is reduced by a factor of 1.57. We call this the 2-parameter approach but it could also be called MLE2. As shown below, while there are significant benefits in terms of range precision by reducing the number of parameters for the CryoSat LRM data, there is no benefit in applying this approach to the SAR-mode data.

The optimal algorithm for retracking CryoSat waveforms (LRM and SAR), as well as ERS-1, Geosat, Envisat, and Jason-1 waveforms, is based on trial and error using tens of ocean tracks. In all cases, the best method is selected based on the median absolute difference between the along-track ocean slope, filtered at 18 km wavelength, and the slope of the ocean surface extracted from the EGM2008 global gravity model [*Pavlis et al.*, 2012]. The parameters to be tuned are the trailing edge decay rate, the form of the power weighting function, and the number of waveforms to assemble into a single least-squares analysis. The optimal trailing edge decay values in $gates^{-1}$ for each of the data types is: 0.006-Geosat; 0.022-ERS-1; 0.090-Envisat; 0.0058-Jason-1; 0.0130-CryoSat/LRM; 0.0149-CryoSat/SAR. The value of this parameter depends mainly on the beam pattern of the radar antenna, the off-nadir pointing angle, and the altitude of the spacecraft. Except in the case of Geosat, which has large off-nadir excursions, we did not attempt to estimate this parameter from the waveform data for two reasons. First, allowing the parameter to vary rapidly along a satellite track will increase the noise in the range precision, which in turn, will increase the error in the final gravity estimate. For example, *Smith et al.* [2011] solved for the trailing edge decay for CryoSat/LRM waveforms. When they mapped these into off-nadir pointing angle, the excursions were three times larger than the measured off-nadir pointing of the spacecraft. The implication is that least-squares estimates of this parameter are not robust. Second we showed above (Figure 5d) that the off-nadir variations vary smoothly over each orbit so the slope error introduced by neglecting this effect will be small. Note that the height error caused by

variations in off-nadir pointing is sometimes significant and should be accounted for when retracking for measuring ocean heights [*Thibaut et al.*, 2010].

The second type of tuning was related to the form of the weight function used in the least-squares analysis. Theoretical considerations [*Brown,* 1977] show that because the ocean surface scattering follows a Rayleigh distribution the noise of the data within the waveform should be proportional to the power. In addition there should be a pre-arrival noise level based on the engineering characteristics of each altimeter. These two parameters were tuned to achieve the best fits between along-track slope and EGM2008 slope for numerous profiles. It is interesting that all the Brown-type waveforms (Geosat, ERS-1, Envisat, Jason-1, and CryoSat/LRM) required a significant downweighting of the higher power data while the CryoSat SAR waveforms had best fits when a uniform weight was used.

The third type of tuning is the number of 20 Hz waveforms to be used in each least-squares adjustment. In a previous study involving ERS-1 [*Sandwell and Smith,* 2005] we found optimal along-track slope fits when three waveforms were used and the two outer waveforms were given ½ the weight of the central waveform. This approach is also optimal for CryoSat/LRM and SAR and we simply adopted the same weighting scheme for Envisat and Jason-1. Note that Geosat waveforms are provided at 10 Hz and we found that fits to single waveforms provided optimal results. Later when the 20-Hz noise levels of each altimeter are presented, the Geosat values will be multiplied by a factor of 1.41 to account for the reduced number of independent waveforms in the least-squares adjustment.

Examples of fits to the three modes of CryoSat data are provided in Figure 6. The left plot shows fits to the LRM data using the 2-parameter Brown model. As described in the *Sandwell and Smith* [2005] study, a two-step retracking approach was used. The data are assembled into continuous tracks of 20-Hz waveforms. A three-parameter retracking is performed during the first pass; then the rise time parameter is smoothed over a ½ wavelength of 45 km and the pass is retracked a second time using this fixed value of rise time. A similar approach is used for the SAR and SARIN data. In all cases the model and the data show good agreement with one notable exception where the “toe” of the SAR and SARIN waveforms is not well matched by the model. As discussed above, this

toe is due to multilooking the SAR waveforms to improve their signal-to-noise ratio. The three lower plots in Figure 6 show the waveform residuals for 100 waveforms in each case. As expected the misfit to the LRM waveform is greater where the power is greater and there is no systematic variation to the misfit. The misfit to the SAR waveform shows a prominent leading edge signature cause by a poor match at the "toe". This analysis does not reveal the precision in the arrival time needed for the gravity field construction.

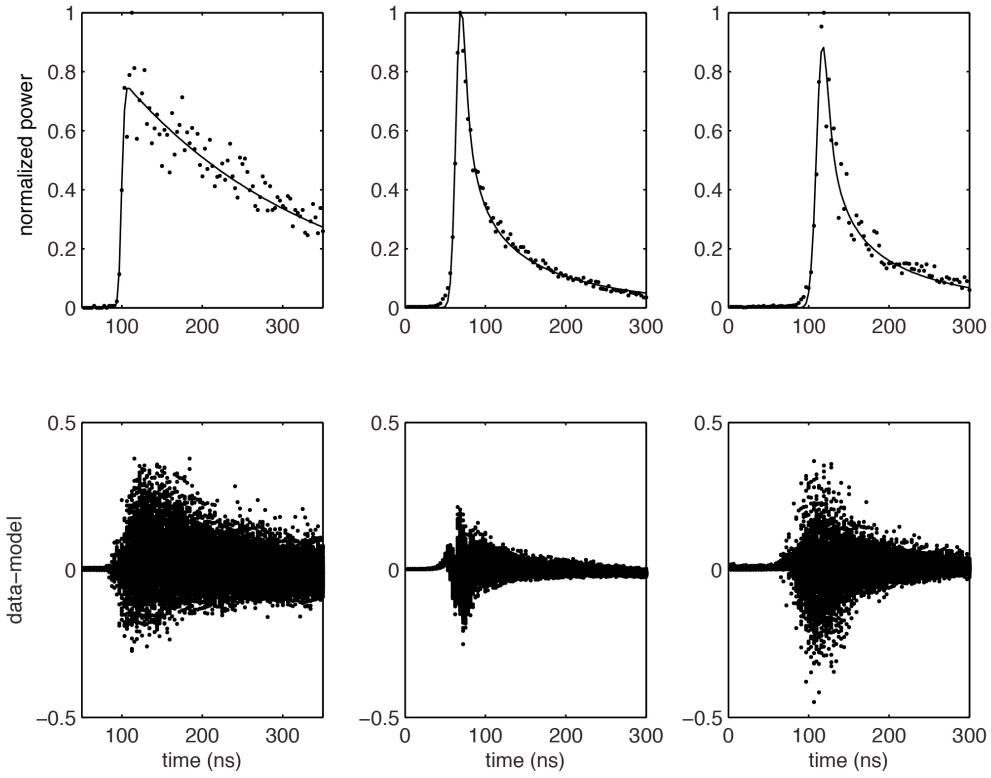

Figure 6. (a) Least squares fit of model waveforms to LRM, SAR, and SARIN data. Residuals shown below are misfits from 1000 waveforms to reveal scatter as well as systematic variations. The SAR model single-look waveform does not match the "toe" in the waveform data resulting in a systematic misfit.

Noise and Coherence

We use two approaches to estimate the noise and spatial resolution of the retracked data. A commonly-used estimate of retracker noise is the standard deviation of the 20Hz range estimates about the 1 Hz mean [*Cheney et al*., 1991; *Gommenginger et al*., 2011]. Rather than using the mean, we converted the range to sea surface height and computed the standard deviation from the EGM2008 model. Using a reference model can be

important in areas of high geoid slope such as the walls of the deep ocean trenches. We selected a rectangular region in the North Atlantic such that the passes collected in the western half were mostly in LRM mode, while the eastern half contained SAR-mode data and plotted this 20 Hz estimate vs SWH (white box in Figure 1). We did the same analysis for Geosat, ERS-1, Envisat, and Jason-1, as shown in Figure 7. This was done for 3-parameter (green dots) and 2-parameter (blue dots) retracking. The solid smoothed curves are median averages of these estimates in 0.4 m SWH bins. Noise estimates of each altimeter at 2 m and 6 m SWH are provided in Table 1.

As expected, the noise level of the SAR data is between 1.8 and 1.3 times better than the other altimeters when all retracking is done using three parameters. For 2 m SWH, our computed value of 49.7 mm differs by less than a 1 mm from those obtained using different SAR waveform retracking approaches [*Giles et al.,* 2012; *Gommenginger et al.,* 2012]. This result is somewhat less than the expected factor of 2 improvement in range precision based on engineering analysis [*Raney et al.,* 2003]. There are two possible reasons why we have not achieved this factor of 2 improvement. First it is possible that our fits to the SAR waveforms are suboptimal because our model does not include the toe-signal caused by multilooking. Second, the factor of 2 improvement was based on an open-loop SAR design where the 18 kHz pulse repetition frequency of the SAR was continuous [*Raney*, 1998]. In the case of CryoSat the radar operates in a burst mode where 64 pulses are emitted and recorded such that the radar is only emitting about 1/3 of the full 18 kHz rate. The more surprising result is that in the case of 2-parameter retracking, the reduction in noise level of the SAR waveforms is small while for the non-SAR data the noise reduction is large and very close to the theoretical noise reduction of 1.57. Indeed, for 2 m SWH the noise of the CryoSat LRM is lowest (42.7 mm), followed by Jason-1 (46.7 mm,) and then CryoSat SAR (49.7 mm). At 6 m SWH Jason-1 has the lowest noise level of 64.2 mm followed by LRM (71.7 mm), Envisat (88.6 mm), and then SAR (110.9 mm). The relatively poor performance of the SAR-mode data at the larger wave heights could reflect the increase in arrival time error with increasing SWH shown in Figure 4 but it could also result from off-nadir wave height noise. It is also notable that the noise levels of the new altimeters (Envisat, Jason-1, and CryoSat) are

significantly lower than the noise levels of the older (Geosat and ERS-1) altimeters. This could be simply due to the nearly factor of 2 increase in PRF in the newer altimeters.

One of the more remarkable findings is that the ratio of 3-parameter noise to 2-parameter noise is largely independent of altimeter and very close to the theoretical value of 1.57 based on a least-squares simulation (Table 1). Later we will perform a similar simulation using the SAR waveform to demonstrate why this two-pass approach is not beneficial for SAR data.

A previously unexplored issue related to this 2-pass retracking method is what part of the wavenumber spectrum benefits most. To explore this issue we computed power spectra along satellite tracks of the difference in height between the 3-parameter and the 2-parameter approach as shown in Figure 8. All the altimeters show elevated power spectral density between the wavelengths of 45 km and 5 km, which has been called a spectral "hump". The fall-off in the difference spectra for wavelengths greater thatn 45 km simply reflects the wavelength over which the SWH was smoothes between the 3-parameter and 2-parameter retracking. At longer wavelengths, both retrackers provide the same height measurement because the profiles contain the same SWH signal. At shorter wavelengths there is a significant filtering of the SWH, so the retrackers provide very different output. At the shorter wavelength end of the difference spectrum between 10 km and 3 km the outputs from the two retrackers also become similar. We speculate that this is due to the finite pulse-limited diameter of the radar footprint. We note that the shortest wavelength available in marine gravity models derived from altimetry is about 12 km so this finite footprint size is not yet a limitation on gravity field resolution.

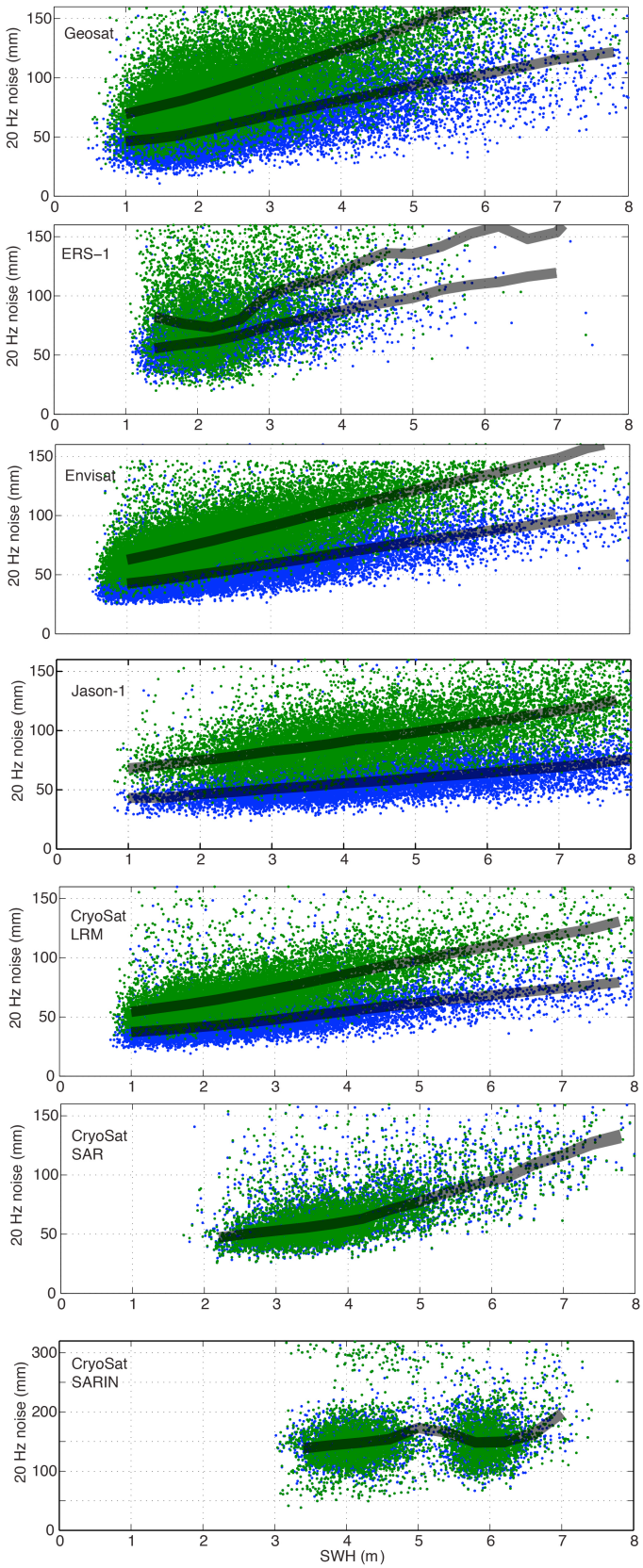
Geosat
ERS−1
Envisat
Jason-1
CryoSat
LRM
CryoSat
SAR
CryoSat
SARIN
20 Hz noise (mm)
SWH (m)

Figure 7 Standard deviation of retracked 20 Hz height estimates with respect to EGM2008 (mean removed) for all geodetic mission altimeter data (Geosat/GM, ERS-1/GM, Envisat 35/30 repeat, and CryoSat LRM, SAR and SARIN. The data are from a region of the North Atlantic with relatively high sea state, white box in Figure 1 except the SARIN data are from the South Atlantic. Green dots are from 3-parameter retracking while blue dots are from 2-parameter retracking (every 10th point plotted). The thick lines are the median of thousands of estimates over a 0.4 m range of SWH. Note the 2- and 3-parameter results are nearly identical for the CryoSat SAR data. The 10Hz Geosat estimates were scaled by 1.41 to approximate the errors in at a higher sampling rate of 20 Hz.

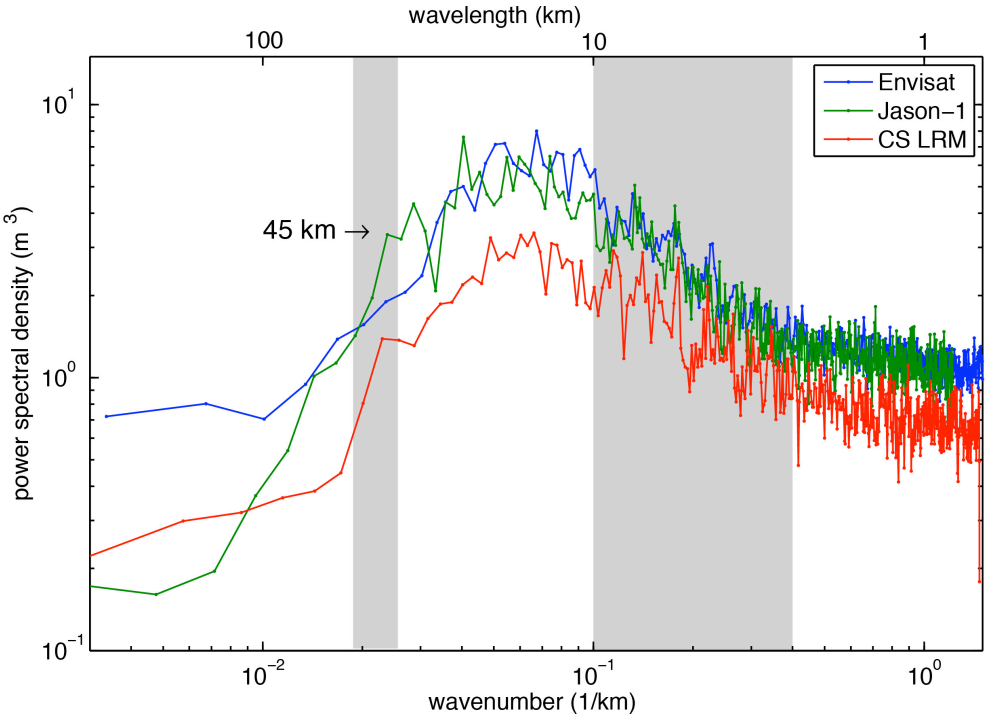

Figure 8 Power spectra of the difference in along track height between passes retracked with the 3-parameter model and the 2-parameter model after smoothing the SWH over a ½ wavelength of 45 km. There is a "hump" in the spectrum between 5 and 45 km where most of the noise reduction occurs.

Table 1. 20 Hz Altimeter Noise (mm)

Altimeter	3-PAR @ 2 m	2-PAR @ 2 m	3-PAR/2-PAR	2 PAR @ 6 m
Geosat	88.0	57.0	1.54	105.4
ERS-1	93.6	61.8	1.51	111.8
Envisat	78.9	51.8	1.52	88.6
Jason-1	75.9	46.4	1.63	64.2
CryoSat LRM	64.7	42.7	1.51	71.7
CryoSat SAR	49.5	49.7	.996	110.9
CryoSat SARIN	138.5	138.7	.998	148.6

Standard deviation of retracked 20 Hz height estimates with respect to EGM2008 (mean removed). The data are from a region of the North Atlantic with relatively high sea state. The values represent the median of thousands of estimates over a 0.4 m range of SWH.

The 10Hz Geosat estimates were scaled by 1.41 to approximate the errors in at a higher sampling rate. Note in all cases except for the CryoSat SAR and SARIN modes, the 3-PAR to 2-PAR noise ratio is close to the 1.57 value derived from a least-squares simulation.

A cross-spectral analysis of repeating altimeter profiles can be used to assess the shortest wavelength resolvable in the along-track slope data [*Marks and Sailor*, 1986]. This is important for designing low-pass filters to be applied to the 20Hz data prior to gravity field construction [*Yale et al.,* 1995]. The spectral coherence between height measurements along repeating profiles is a measure of the ratio of the common geoid signal to the time varying oceanographic noise, as a function of spatial wavelength. The value of coherence is close to 1 at longer wavelengths where the signal dominates, and is small (< 0.2) where the noise dominates [*Bendat and Piersol,* 1986]. A conservative estimate of the effective resolution of the along-track data is given by the wavelength at which the coherence level is 0.5.

We selected ground tracks within a region in the North Atlantic Ocean and assembled pairs that repeat to within about 1 kilometer apart. This set of tracks included both LRM and SAR mode data, and we performed the coherence analysis separately for each mode. For data from both modes, results from 2-parameter retracking were used to compute the along-track slopes. To obtain statistically significant coherence estimates we used Welch's modified periodogram method on multiple passes. The data were pre-whitened by taking the along-track derivative, resulting in along-track slope. The resulting coherence curves are shown in Figure 8. We found that LRM slope acquisitions have a resolution limit of 27 kilometers, while for SAR, this was at 26 kilometers. In comparison, previously published values using a similar analysis in another area of the Atlantic quote a 33-kilometer resolution for Geosat, and 33-kilometer resolution for ERS-1 [*Yale et al*, 1995]. These preliminary results suggest that the spatial resolution of CryoSat-derived gravity will be at least 1.2 times better than previous models.

The power spectrum of the SWH has a change in trend at a wavelength of 45 km (see Figure 4b). This reflects the wavelength where the noise in the estimation of SWH is larger than the SWH signal. For ERS-1 the break in the spectrum occurred at ~90 km [*Sandwell and Smith*, 2005]. We used this as the filter wavelength to smooth the SWH

before 2-parameter retracking. This analysis suggests that we could do less smoothing for the CryoSat data because the SWH is more accurately determined. This will provide better results in areas where there is a spatially rapid variation in swell height.

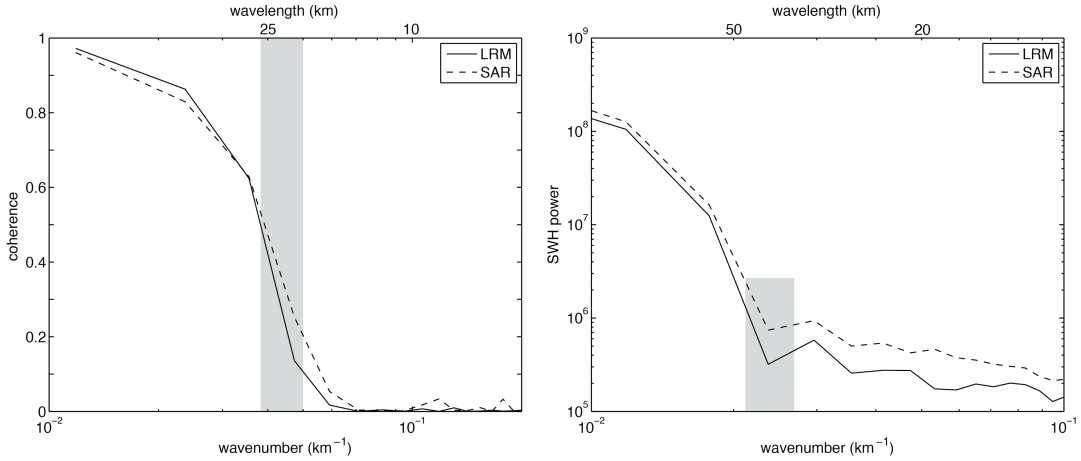

Figure 9 (a) Coherence versus spatial wavenumber (wavelength) for repeat along-track slope profiles in the North Atlantic (white box in Figure 1). The LRM/SAR coherence falls to a value of 0.5 at a wavelength of 27 km / 26 km and a value of 0.2 at a wavelength of 22 km / 20 km. (b) Power in SWH versus wavenumber (wavelength) for 3-parameter retracking of LRM (solid) and SAR (dashed).

Correlated Model Errors

The big surprise in this analysis is that the 20 Hz range precision and along-track coherence are very similar for the CryoSat SAR and LRM modes when the LRM is retracked at 2 parameters. To investigate why this happens in the least squares fitting one can examine the 3x3 covariance matrix which provides the relative uncertainties in the accuracy of the estimated parameters as well as their cross correlations. The results are provided in the table below where the covariances were scales so the arrival-time variance is one. The analysis was done for both the LRM and SAR modes for SWH of 2 m and 6 m. In general the SWH is more accurately estimated for the SAR than for the LRM (i.e. sigma-sigma term). More important the cross correlation between sigma and tau is relatively large for the LRM (0.27 @ 2m SWH and 0.43 @ 6 m SWH. In contrast the cross correlation between sigma and tau is smaller for the SAR (0.11 @ 2 m SWH and 0.19 @ 6 m SWH).

	LRM				SAR		
2 m	0.0678	0.1324	0.1379		0.1505	0.0714	0.2348
		1.0000	0.2694			1.0000	0.1115
			1.3947				1.0644
	A	τ	σ		A	τ	σ
6m	0.0441	0.1381	0.1392		0.0662	0.0749	0.1682
		1.0000	0.4356			1.0000	0.1903
			1.3489				1.0832

Comparison with EGM2008

Thus far we have evaluated the quality of the various altimetry data sets that are used to construct the marine gravity field by examining the noise and spectral characteristics of the slope measurements along the satellite ground tracks. Another way of evaluating the performance is by comparing it with another gravity model. We accomplish this by differencing altimeter slope profiles with those computed from the Earth Gravitational Model 2008 (EGM2008) [*Pavlis et al*., 2012]. This is a model of the Earth's gravitational potential that is complete up to spherical harmonic degree and order 2159, resulting in an effective resolution of 5 arc-minutes at the sea surface. EGM 2008 merges data from satellite gravity (the ITG-GRACE03S model, produced using data from the Gravity Recovery and Climate Experiment mission), as well as terrestrial, altimetry-derived, and airborne free-air gravity surveys. The root mean square of the slope differences between these gravity data sets provides a way to quantify the magnitude of the errors of the altimeter profiles as well as to characterize their spatial distribution across the global ocean.

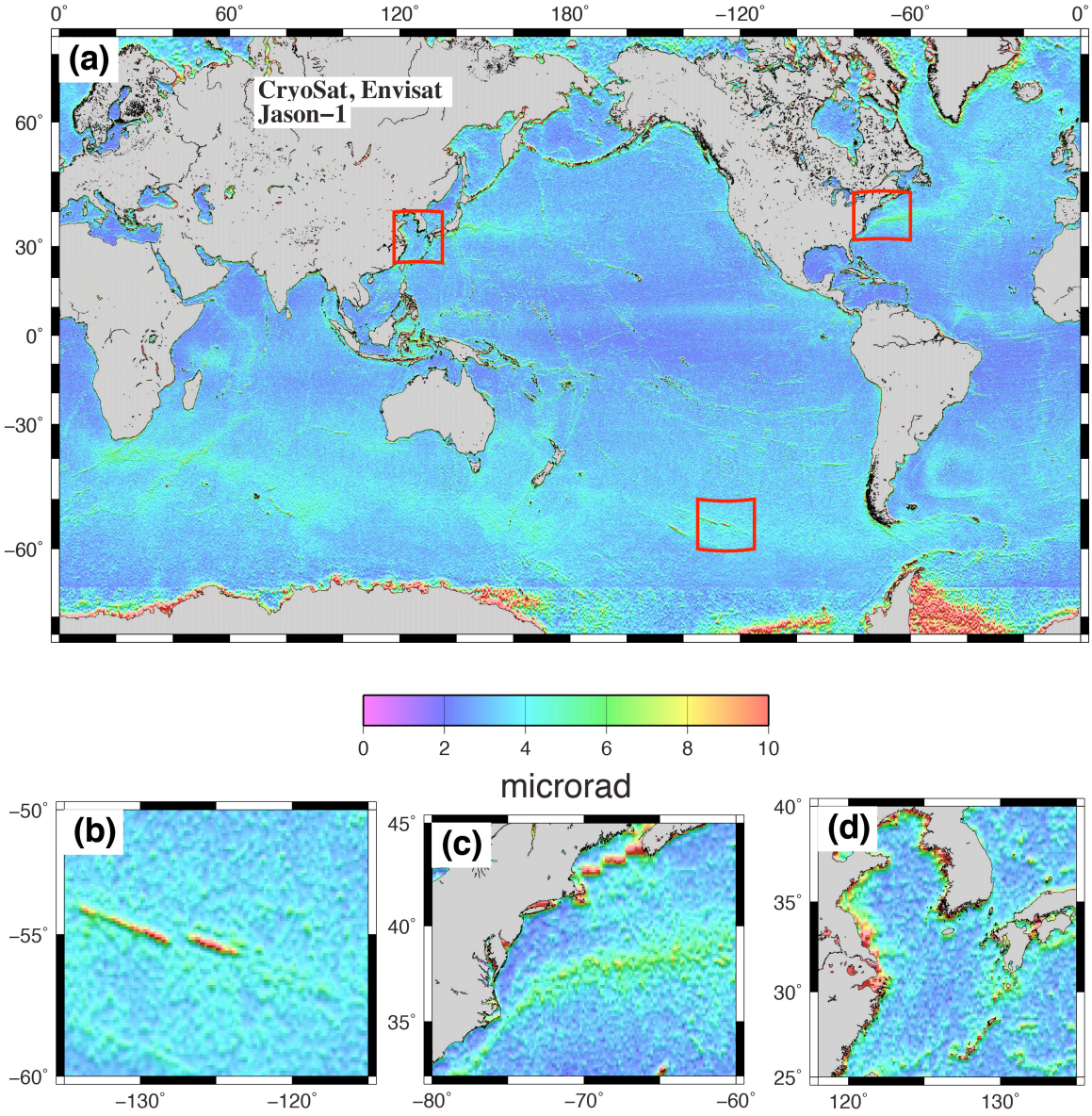

Figure 10. (a) RMS differences between slopes from EGM 2008 and those from profiles collected from the CryoSat, Envisat, and Jason-1 missions across the global ocean. Note the relatively higher errors concentrated in a latitudinal band in the southern hemisphere. Other examples of areas with high noise include those with (b) steep seafloor topography, (c) mesoscale variability associated with ocean surface circulation, and (d) shallow coastal regions where tide models are prone to errors (see text for further discussion).

In figure 10 we show maps of these RMS differences between CryoSat, Envisat, and Jason-1 along-track slopes and those from EGM2008. A low-pass filter with a 0.5 gain at 12 km wavelength was applied to the difference profiles. After filtering, the RMS differences were averaged in 0.20° cells. For all altimeter data sets, there are several

common patterns of high noise areas that stand out from the background level of about 2 microradians (tinted blue on the map) that is prevalent across the deep and open ocean. These have different geophysical sources, namely: sea surface roughness due to wind waves, sharp tectonic features, mesoscale ocean variability, and sea ice cover.

Prevalence of stormy weather between 60° S and 30° S leads to high winds and large amplitude waves, inducing greater radar ranging error and thus impaired slope retrieval. Meanwhile, in areas of large amplitude, small-scale, seafloor topography such as at the global spreading ridge system, over large seamount crests, and fracture zone offsets (Figure 10b), sharp changes in the slope are not captured by the EGM2008 model. There are also some areas of higher slope error in regions that are adjacent to persistent surface circulation patterns associated with boundary currents such as the Gulf Stream (Figure 10c), the Kuroshio, and the Agulhas Current, as well as the equatorial circulation in the Pacific and the Antarctic Circumpolar Current. While there is a dynamic ocean topography model incorporated in EGM2008 that partly accounts for global ocean circulation patterns, it does not compensate for mesoscale variability that is a consequence of meandering currents and eddies.

Meanwhile, for the polar regions that are encompassed by the CryoSat and Envisat observations, another source of slope error is due to the shifting sea ice cover. This could, however, be potentially addressed by adopting a waveform processing scheme that discriminates between sea ice and open ocean returns, and selects different retracking techniques that are optimized for each case.

Higher discrepancies among slopes from altimetry and EGM 2008 are also present for coastal regions with shallow (< 1 km) bathymetry, especially at continental shelves (Figure 10d). In this case, the error in the altimeter measurements results from corrections for the contributions of the tides to the sea surface heights. This could be addressed by employing more accurate and higher-resolution tidal models that are suitable for coastal applications.

Conclusions

To measure marine gravity anomalies at an accuracy under 1 mGal, the error in the along-track slopes from the altimeter profiles must be about 1 μrad, or there must be

enough repeated tracks to achieve the 1 μrad accuracy. This study compiles several contributions towards this goal.

We have shown that a simple analytic function, which we derived to model CryoSat SAR-mode waveforms, performs well in estimating along-track sea surface slope. An intercomparison with simulations conducted by the SAMOSA project, we have demonstrated that for small off-nadir mispointing in the roll direction (< 0.12°), and moderate sea surface roughness (< 6 m), our model is capable of estimating slopes with under 1 μrad of error. This is in spite of the fact that the model does not account for the multilook averaging used to assemble the SAR waveforms. We then calculated the range precision at 20 Hz for a large set of altimeter profiles collected in SAR mode and found that it was almost two times better than earlier noise levels for ERS-1 and Geosat.

Two-pass retracking was originally developed specifically for ERS-1 data [*Sandwell and Smith*., 2005], but we have established that this method also results in a factor of 1.5 improvement in precision for pulse-limited altimetry waveforms for all three new satellite missions. Meanwhile, almost no noise reduction was seen in the CryoSat SAR and SARIN-mode data. This may be attributed to the differences in the nonlinear models used for these modes and that for conventional waveforms. To validate our sea surface slope measurements, a comparison was conducted with the comprehensive, high-resolution EGM2008 spherical harmonic model, and the results show excellent correspondence. Various forms of spectral analyses were also carried out. These all demonstrate that observations from CryoSat, Envisat, and Jason-1 are not only suitable for the recovery of sea surface slopes, but unequivocally offer significant advantages over data from preceding altimetry missions.

Acknowledgements

The CryoSat and Envisat data were provided by the European Space agency, and NASA/CNES provided data from the Jason-1 altimeter. This research was supported by ConocoPhillips, the National Science Foundation (OCE-1128801), and the Office of Naval Research (N00014-12-1-0111). We thank Salvatore Dinardo of ESA ESRIN for providing simulation results for the CryoSat SAR waveforms from the SAMOSA project.

References

Amarouche, L., Thibaut, P., Zanife, O.Z., Dumont, J.-P., Vincent, P. & Steunou, N., 2004. Improving the Jason-1 Ground Retracking to Better Account for Attitude Effects. *Marine Geodesy*, **27**(1-2), pp.171-197.

Andersen, O.B., Knudsen, P. & Berry, P.A.M., 2009. The DNSC08GRA global marine gravity field from double retracked satellite altimetry. *Journal of Geodesy*, **84**(3), pp.191-199.

Bendat, J.S. & Piersol, A.G., 1986. *Random Data---Analysis and Measurement Procedures*. New York: Wiley & Sons. 566 pp. 2nd ed.

Brown, G., 1977. The average impulse response of a rough surface and its applications. *IEEE Transactions on Antennas and Propagation*, **25**(1), pp.67- 74.

Cheney, R.E., Doyle, N.S., Douglas, B.C., Agreen, R.W., Miller, L., Timmerman, E.L. & McAdoo, D.C., 1991. *The Complete Geosat Altimeter GDR Handbook*, National Geodetic Survey, NOAA, Rockville, Md.

Cotton, P.D., Andersen, O., Berry, P., Cipollini, P., Gommenginger, C., Martin-Puig, C., Stenseng, L., Benveniste, J. & Dinardo, S., 2010. The SAMOSA Project: Assessing the Potential Improvements offered by SAR Altimetry Over the Open Ocean, Coastal Waters, Rivers and Lakes. In proceedings of *ESA Living Planet Symposium, June 28 – July 2, 2010*.

Ford, P.G. & Pettengill, G.H., 1992. Venus Topography and Kilometer-Scale Slopes. *Journal of Geophysical Research*, **97**(E8), p.13103.

Fu, L.-L. & Cazenave, A. 2000. *Satellite altimetry and earth sciences a handbook of techniques and applications*, San Diego: Academic Press.

Giles, K., Wingham, D., Cullen, R., Galin, N., & Smith, W.H.F., 2012. Precise Estimates of Ocean Surface Parameters from CryoSat. In proceedings of *Ocean Surface Topography Science Team Meeting. Venice-Lido, September 27-28, 2012*.

Gommenginger, C., Martin-Puig, C., Dinardo, S., Cotton, P.D., Srokosz, M. & Benveniste, J., 2011. Improved altimetric accuracy of SAR altimeters over ocean. In proceedings of *Ocean Surface Topography Science Team Meeting. San Diego, October 19-21, 2011*.

Gommenginger, C., Cipollini, P., Cotton, P.D., Dinardo, S., & Benveniste, J., 2012. Finer, Better, Closer: Advanced capabilities of SAR altimetry in the open ocean and the coastal zone. In proceedings of *Ocean Surface Topography Science Team Meeting. Venice-Lido, September 27-28, 2012*.

Gradshteyn, I.S., 1980. *Table of Integrals, Series, and Products* Corr. and enl. ed., New York: Academic Press.

Hayne, G., 1980. Radar altimeter mean return waveforms from near-normal-incidence ocean surface scattering. *IEEE Transactions on Antennas and Propagation*, **28**(5), pp.687–692.

Jensen, J.R., 1999. Angle measurement with a phase monopulse radar altimeter. *IEEE Transactions on Antennas and Propagation*, **47**(4), pp.715–724.

Louis, G., Lequentrec-Lalancette, M-F., Royer, J-Y., Rouxel, D., Geli, L., Maia, M., & Failot, M., 2010. Ocean Gravity Models from future satellite missions, *Eos,* 91(3), pp. 21-28.

Marks, K.M. & Sailor, R.V., 1986. Comparison of GEOS-3 and SEASAT Altimeter Resolution Capabilities. *Geophysical Research Letters*, **13**(7), p.697.

Maus, S., Green, C.M. & Fairhead, J.D., 1998. Improved ocean-geoid resolution from retracked ERS-1 satellite altimeter waveforms. *Geophysical Journal International*, **134**(1), pp.243-253.

Pavlis, N.K., Holmes, S.A., Kenyon, S.C., & Factor, J.K., 2012. The development and evaluation of the Earth Gravitational Model 2008 (EGM2008), *J. Geophys. Res., 117*, B04406, doi:10.1029/2011JB008916.

Phalippou, L. & Enjolras, V., 2007. Re-tracking of SAR altimeter ocean power-waveforms and related accuracies of the retrieved sea surface height, significant wave height and wind speed. In Geoscience and Remote Sensing Symposium. *IGARSS 2007. IEEE International*. pp. 3533-3536.

Raney, R.K., 1998. The delay/Doppler radar altimeter. *IEEE Transactions on Geoscience and Remote Sensing,* **36**(5), pp.1578–1588.

Raney, R.K., Smith, W.H.F. & Sandwell, D.T., 2003. Abyss-Lite: improved bathymetry from a dedicated small satellite delay-Doppler radar altimeter. In proceedings of *Geoscience and Remote Sensing Symposium Proceedings, IGARSS*, pp. 1083-1085.

Sandwell, D.T. & McAdoo, D.C., 1990. High-Accuracy, High-Resolution Gravity Profiles From 2 Years of the Geosat Exact Repeat Mission. *Journal of Geophysical Research*, **95**(C3), pp.3049-3060.

Sandwell, D.T. & Smith, W.H.F., 2009. Global marine gravity from retracked Geosat and ERS-1 altimetry: Ridge segmentation versus spreading rate. *Journal of Geophysical Research*, **114**(B01411).

Sandwell, D.T. & Smith, W.H.F., 2005. Retracking ERS-1 altimeter waveforms for optimal gravity field recovery. *Geophysical Journal International*, **163**(1), pp.79-89.

Smith, W.H.F., 2004. Introduction to This Special Issue on Bathymetry from Space. *Oceanography*, 17(1), pp. 6-7.

Smith, W.H.F. & Scharroo, R., 2011. Retracking range, SWH, sigma-naught, and attitude in CryoSat conventional ocean data. In proceedings of *Ocean Surface Topography Science Team Meeting. San Diego, October 19-21, 2011.*

Smith, W.H.F., Scharroo, R., Lillibridge, J.L. & Leuliette, E.W., Retracking CryoSat waveforms for near-real-time ocean forecast products, platform attitude, and other applications. In *American Geophysical Union, Fall Meeting 2011.* San Francisco, p. abstract *# C53F-06.*

Stewart, R.H., 1985. *Methods of satellite oceanography*, University of California Press, Berkeley.

Temme, N.M., 2012. Section 12.8. *Digital Library of Mathematical Functions*. Release date: 2012-03-23. National Institute of Standards and Technology from http://dlmf.nist.gov/

Thibaut, P., Poisson, J.C., Bronner, E., & Picot, N., 2010. Relative Performance of the MLE3 and MLE4 Retracking Algorithms on Jason-2 Altimeter Waveforms. *Marine Geodesy*, **33**, pp.317-335.

Walsh, E.J., Uliana, E.A. & Yaplee, B.S., 1978. Ocean wave heights measured by a high resolution pulse-limited radar altimeter. *Boundary-Layer Meteorology*, **13**(1-4), pp.263-276.

Wingham, D., Francis, C.R., Baker, S., Bouzinac, C., Brockley, D., Cullen, R., de Chateau-Thierry, P., Laxon, S.W., Mallow, U., Mavrocordatos, C., 2006. CryoSat: A mission to determine the fluctuations in Earth's land and marine ice fields. *Advances in Space Research,* **37**(4), pp.841-871.

Wingham, D.J., Phalippou, L., Mavrocordatos, C., & Wallis, D., 2004. The mean echo and echo cross product from a beamforming interferometric altimeter and their application to elevation measurement. *IEEE Transactions on Geoscience and Remote Sensing*, **42**(10), pp.2305-2323.

Yale, M.M., Sandwell, D.T. & Smith, W.H.F., 1995. Comparison of along-track resolution of stacked Geosat, ERS 1, and TOPEX satellite altimeters. *Journal of Geophysical Research*, **100**(B8), p.15117.